

Customizable and highly sensitive 3D micro-springs produced by two-photon polymerizations with improved post-treatment processes

Cite as: Appl. Phys. Lett. **120**, 171107 (2022); <https://doi.org/10.1063/5.0088481>

Submitted: 17 February 2022 • Accepted: 11 April 2022 • Published Online: 26 April 2022

Xinggong Shang, Ning Wang, Zimeng Wang, et al.



View Online



Export Citation



CrossMark

ARTICLES YOU MAY BE INTERESTED IN

[Elliptical-tube off-beam quartz-enhanced photoacoustic spectroscopy](#)

Applied Physics Letters **120**, 171101 (2022); <https://doi.org/10.1063/5.0086697>

[Generation of intense sub-cycle terahertz pulses with variable elliptical polarization](#)

Applied Physics Letters **120**, 171106 (2022); <https://doi.org/10.1063/5.0086309>

[30-kHz linewidth interband cascade laser with optical feedback](#)

Applied Physics Letters **120**, 171109 (2022); <https://doi.org/10.1063/5.0090937>

Trailblazers. New

Meet the Lock-in Amplifiers that measure microwaves.

Zurich Instruments [Find out more](#)

Customizable and highly sensitive 3D micro-springs produced by two-photon polymerizations with improved post-treatment processes

Cite as: Appl. Phys. Lett. **120**, 171107 (2022); doi: [10.1063/5.0088481](https://doi.org/10.1063/5.0088481)

Submitted: 17 February 2022 · Accepted: 11 April 2022 ·

Published Online: 26 April 2022





View Online



Export Citation



CrossMark

Xinggong Shang,^{1,2,3} Ning Wang,^{2,3,a)} Zimeng Wang,⁴ Hanqing Jiang,^{2,3}  Yunfei Jia,^{4,a)} Nanjia Zhou,^{2,3,a)} and Min Qiu^{2,3,a)} 

AFFILIATIONS

¹College of Optical Science and Engineering, Zhejiang University, Hangzhou, China

²Key Laboratory of 3D Micro/Nano Fabrication and Characterization of Zhejiang Province, School of Engineering, Westlake University, 18 Shilongshan Road, Hangzhou, Zhejiang, China

³Institute of Advanced Technology, Westlake Institute for Advanced Study, 18 Shilongshan Road, Hangzhou, Zhejiang, China

⁴Key Laboratory of Pressure Systems and Safety, Ministry of Education, School of Mechanical and Power Engineering, East China University of Science and Technology, Shanghai, China

^{a)}Authors to whom correspondence should be addressed: wangning@westlake.edu.cn; yfjia@ecust.edu.cn; zhounanjia@westlake.edu.cn; and qiu_lab@westlake.edu.cn

ABSTRACT

Springs are ubiquitous in a variety of scientific and engineering fields. However, the comprehensive study on mechanical properties of micro-spring has not been fully conducted yet due to a lack of reliable productions of varied-shaped micro-springs. Here, we report the design and manufacturing of triple-helix-shaped springs employing two-photon polymerization (TPP) technologies and present a systemic study on the mechanical properties of micro-springs particularly involving spring constants of k . To construct high-quality hollow micro-structures, we optimize the TPP process by combining violet light post-treatment with a proper selection of cleaning liquid. Consequently, we demonstrate that the sensitives k can be actively tuned over a range of two orders of magnitude, from ~ 1.5 to $\sim 108.2 \mu\text{N}/\mu\text{m}$ while maintaining a high resolution of $\sim 1 \mu\text{N}/\mu\text{m}$. Furthermore, compression tests showcase an excellent agreement among all force-vs-displacement lineshapes, resulting in a small k fluctuation of $< 1\%$. On the whole, we expected that the modified TPP technique along with proposed helical springs opens an alternative avenue toward micro-scale force detection, leading to potential applications in the field of bio-sensing, where typical forces to be measured exist within a broad range from several piconewtons to several micronewtons.

Published under an exclusive license by AIP Publishing. <https://doi.org/10.1063/5.0088481>

The mechanical spring is one of the most-known physical structures in everyday use. A dominant feature of compression springs lies in the sensing constant of k , which follows Hooke's law of $F = -k \cdot x$, with F and x being applied force and displacement, respectively.¹ At the macroscale, steel-based coil springs are commonly manufactured by well-established industrial coiling machines. However, at the micro-scale, significant challenges still exist to implement 3D helical springs since majorities of lithographical engineering processes best suit planar 2D patterns.^{2–6}

Recent advances in direct laser writing [i.e., two-photon polymerization (TPP)] represents a versatile tool for the productions of 3D

structures.^{7–9} As an additive manufacturing technology, TPP could form highly cross-linked polymers that are triggered by the nonlinear absorption typically via femtosecond (fs) pulsed laser.^{10–13} In principle, TPP allows for the creations of nearly any arbitrary-shaped objects with feature sizes down to sub-micrometer, which has been applied to a variety of frontier research fields, including but not limited to, microelectromechanical systems (MEMS),¹³ biosensing,¹⁴ and metamaterials.¹⁵ While current liquid evaporation process after TPP would induce structural deformations¹⁶ and, in the worst case, the complete collapse of the hollow springs. To improve the object stiffness, two types of modifications on TPP are currently employed. On the one hand, an intuitive and

common way to ease fabrication difficulties is to increase the characteristic size (e.g., by enlarging the coil inner radius). On the other hand, setting up external scaffolds would reinforce the hollow springs to avoid structure subsidences as well.^{17–20} However, either way will inevitably modify the mechanical property of springs, especially the latter introduces additional structural complexities and limits original mechanical features. To date, it remains a challenge to realize arbitrary-shaped springs at will. Hence, comprehensive investigations on the mechanical properties of micro-springs have not been systematically conducted yet, and the micro-spring-based force-sensinstrumentation awaits further development.

Therefore, to overcome the fabrication bottleneck, the improved TPP technique targeted for helical springs is first investigated in this report. To fix printing failures, we optimize the development and cleaning process using violet light (405 nm) together with a low surface tension cleaner. Then, real-time characterizations are adopted via an *in situ* nano-indentor. The scanning electron microscope (SEM) images capture the uniformed compression of a triple-helix platform, where the stress distributions are analyzed accordingly through finite-element simulations. Subsequently, the mechanical properties, particularly including sensitives, k , are discussed in-depth. The exceptional designability of the helical microstructure is demonstrated via a set of experimental pieces of evidence, where the k values approach the identical levels of AFM tips. Finally, a conclusion and an overview of potential applications are given.

Overall, the optimized TPP fabrication process is outlined in Fig. 1(a) in the order of substrate cleaning, photoresist dipping, TPP printing, and development with post-cleaning. A schematic of a spring stands on the right, which consists of three helixes topped with a flat cap. The geometrical parameters are specifically listed as the outer radius R , height H , composite coil width w , and associated thickness t (see the cross section in the red box). Note that structure geometries (e.g., helix numbers of N , coil turn numbers n , corresponding cross sections geometry, cap shapes, etc.) and mentioned parameters can be, in particular, customized according to the sensing demands.

The detailed improvements are presented in Fig. 1(b). Here, a drop of photoresist (IP-Dip) is placed on an ultrasomic-cleaned fused silica substrate and then transferred to a commercial TPP equipment (Nanoscribe GmbH PPGT2). Prior to printing, the spring sketch was first drawn in a 3D modeling program and further processed via describe to obtain a gwl file. For detailed configurations, GalvoMode was chosen as the XY-plate scan mode, and an oil-immersion objective lens (63 \times , NA = 1.4) with ultraprecise piezo actuators were employed for high-resolution printing. The scanning speed of 200 $\mu\text{m/s}$ and laser power of 20 mW (wavelength: 780 nm) were, in particular, optimized for the best outputs of micro-springs. After TPP printing and sample exposures, it is further developed in a bath of propylene glycol methyl ether acetate (PGMEA) for at least 10 minutes in order to eliminate the uncured photoresist. Now a split procedure appears at the key step of resist-cleaning to compare the normal cleaning procedure with our modified one. On the upper panel, the conventional treatment is common to utilize an isopropanol (IPA, surface tension $\sigma = 22 \text{ mN/m}$ ²³) bath to eliminate the PGMEA, leaving clean object surfaces. However, fully preserving open-celled helixes over the evaporation and multiple rinsing is significantly more challenging compared to bulk structures. The interfacial tension of the cleaning solvent is

typically greater than the resistance of the printed IP-Dip material. The enlarged caps introduce additional weights that may bring down the lower springs as well. All these factors result in object deformations or, even worse, total collapses of printed springs [see the upper image in Fig. 1(b)].

Here, we optimize the post-processing procedures of hollow objects as indicated by green arrows in Fig. 1(b). Generally speaking, the criterion considered for producing fragile structures is to decrease the interfacial tension.^{24,25} Therefore, a cleaner (i.e., methyl nonafluorobutyl ether, $\text{C}_5\text{H}_3\text{F}_9\text{O}$) is carefully selected owing to its lower surface tension of $\sigma = 14.13 \text{ mN/m}$.²⁶ Concurrently, the structure is exposed to violet light for 15 min¹⁶ in order to improve the stiffness of printed materials. Following this improved cleaning step, a well-maintained helical geometry is created as can be seen from the orange-framed focused helium ion microscopy (FHIM) image in Fig. 1(b). Here, the spring (R : $\sim 25 \mu\text{m}$, H : $\sim 40 \mu\text{m}$) composed of three slim helixes (w : $\sim 3.0 \mu\text{m}$, t : $\sim 2.5 \mu\text{m}$, and N : 3, n : 1) highlights the superb printing capabilities of our approach.

Note that, in principle, this modified method could be applied to other types of delicate structures featuring characteristics like hollow core or high aspect ratio (AR) as well. Displayed on the left hand of Fig. 1(c), eight different micro springs varying parameters of either R (upper panel, from 12 to 18 μm with a step size of 2 μm) or w (lower panel, increasing from 4 to 7 μm by an interval of 1 μm) showcase the wide fabrication applicability and diversity. More images on an array of 4×4 identical springs [same geometries as Fig. 1(b)] can be seen in [supplementary material](#). And gradually increased pillars on the right reaches a high AR (defined as pillar height over its diameter) of ~ 9 , representing an excellent demonstration that the improved TPP could produce various types of high-quality microstructures.

For fair assessment, recent literature on spring-like micro-objects developed by TPP has been summarized in Table I.^{17–22} Here, to evaluate the spring structural fineness, a characteristic size (S) normalized to composite helix number (N) is defined as $S = S_{cap} / (N \cdot S_{cross-section})$, where S_{cap} and $S_{cross-section}$ indicates cap surface area and coil cross section size, respectively. As we showcased in Fig. 1(b), one of major challenges to produce such hollow micro-structures lies in the weight or size of topped caps (i.e., the larger caps mean the better springs). Hereby, the proposed factor should best represent the free-standing springs' geometrical characteristics, which is tightly related to the overall size of upper caps. As shown in Table I, our optimized TPP yields the highest characteristic size (>87) among all references, and the substance appearance comparisons emphasize our spring's great uniformity and fabrication consistency. Note that majority of micro-springs listed in Table I are actually developed by commercial TPP machines utilizing same materials. In this sense, our optimized technique should represent best results under same context by now. Since there is no external reinforcing support, our springs could exhibit "unchanged" mechanical properties. Hence, we conclude that the optimized TPP provides an alternative solution for high-resolution photonic 3D fabrications and further broaden direct laser writing's utilization on fragile micro/nano-structures.

To identify the mechanical property of springs, all the characterizations are carried out utilizing an *in situ* quantitative nano-indentor (Hysitron TM PI88) equipped with an SEM (Zeiss Crossbeam 340). For better visualization purpose, the sample table was tilted and rotated 45°. Note that, the force baseline leveling was arranged to decrease the influence of the weight of the indentor. Three real-time

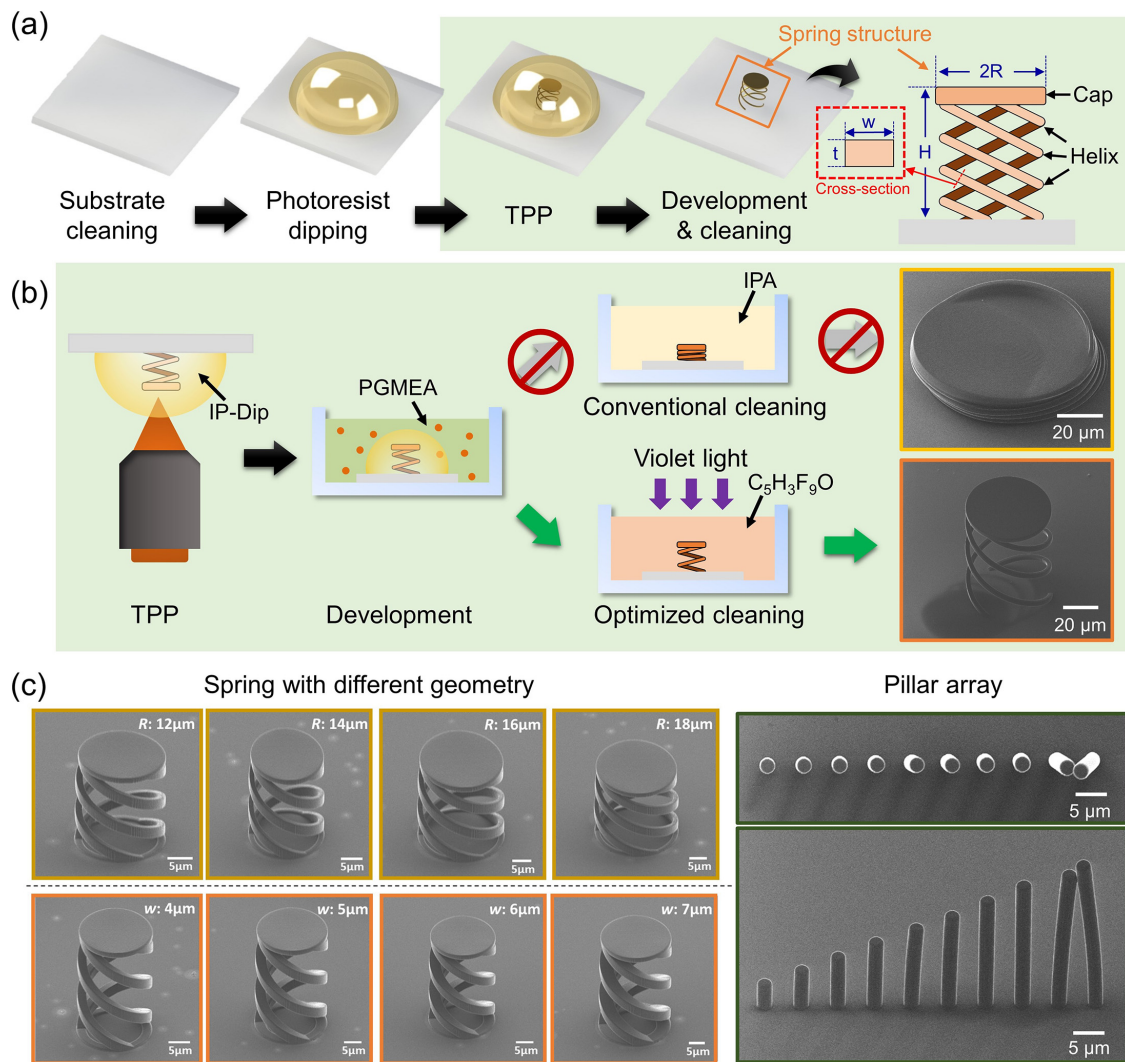


FIG. 1. Optimized two-photon polymerization (TPP) techniques for fabricating micro-springs. (a) An overview of the modified TPP pipeline with a sketch showing the helical geometry. (b) The improved resist development and cleaning procedures (lower panel) in comparison with conventional treatments (upper panel). On the right side, focused helium ion microscopy (FHIM) image in a yellow frame displays a collapsed object induced by the traditional cleaning, while the orange-framed graph exhibits a well-engineered helical spring ($R: 25 \mu\text{m}$, $H: 40 \mu\text{m}$, $w: 3.0 \mu\text{m}$, $t: 2.5 \mu\text{m}$, $N: 3$, $n: 1$) after proper post-processing optimizations. (c) TPP-produced springs (left) and pillar array (right) showing the exceptional fabrication quality. From left to right, the R values of the upper four springs are modified from 12 to 18 μm (step size: 2 μm), while the w of lower four springs is changed from 4 to 7 μm (step size: 1 μm).

images extracted from one complete test are presented in Fig. 2(a), divided into three steps as probe calibration (black-framed with a label of “i”), spring compression (orange-framed with a label of “ii”), and recovery (blue-framed with a label of “iii”), respectively. A cone tip (tip radius: 2.5 μm) pushes and pulls the center of the cap at a constant speed of 100 nm/s, and the upper limit of applied displacement (the distance between the orange line and blue line) is set to 5 μm . For this specific triple-helix structure, three key parameters of R , w , and t are designed as 15, 7, and 4 μm , respectively. Note that over the three phases, the spring must be vertically positioned since any inclinations may cause significant errors. In comparison between phase “i” and “iii,” the cap almost fully returned to its initial position and there are

no visible appearance changes on the helical structure (e.g., no damage on the coils and cap).

Figure 2(b) reflects a correlation between applied displacement and detected force. Two colored lines and Roman numerals correspond to the characterization steps in Fig. 2(a). Here, it is assumed that the helix movement follows general Hooke’s law. The hysteresis between the orange and blue curves can be attributed to several factors including nano-indenter characterizations (e.g., see a case of metal micro-springs²⁷) materials viscoelasticity as well as structural characteristics, where the detailed investigations are beyond this scope of interest. While the great recovery ability of springs could be truly observed in [supplementary material](#) video alongside the multiple cycle

TABLE I. Comparisons of TPP-based techniques for spring-like hollow structures.

References	Geometry features					General structural evaluation			
	helix number	Coil radius R (μm)	Cap geometry and size (μm^2)	Cross section shape and size (μm^2)	Normalized characteristic size	Additional scaffold	Structure orientation	Structure uniformity	Remarks
17	3	~ 5	Flat disk, ~ 78.5	Round, ~ 9.6	2.7	Yes	Vertical	Good	...
18	1	~ 10	...	Round, ~ 0.785	...	Yes	Horizontal	Good	Preserved in gel matrix
19	3	~ 25	Flat disk, ~ 1963.5	Rectangle, ~ 64	10.2	Yes	Vertical	Good	...
20	1	~ 15	Flat disk, ~ 706.5	Round, ~ 19.625	36	Yes	Vertical	Good	Collapses of isolated springs
21	1	~ 1	Bead, ~ 3.1	Round, ~ 0.1256	25.1	No	Vertical	Visible inhomogeneous coil pitch	Easy to be tilted
22	1	~ 44	Flat disk, ~ 6082.1	Round, ~ 572	10.6	No	Vertical	Good	Easy to be tilted
This work	3	~ 25	Flat disk, ~ 1963.5	Rectangle, ~ 7.5	87.3	No	Vertical	Good	Good stability

tests in Fig. 4 (i.e., the cap nearly backs to the original positions). We define the linear fit value over the loading curve as the sensitivity of k (unit: $\mu\text{N}/\mu\text{m}$) to evaluate the force-sensing features, that is also applied for the following analysis in Figs. 3 and 4.

Furthermore, the stress distributions under identical compression scenarios of Fig. 2(a) are numerically simulated for overall studies on structure deformations, which was carried out by COMSOL multiphysics, employing a module of structural mechanics. The material parameters including, e.g., Young's modulus and Poisson's ratio were taken from Ref. 21. A face pressure source was adopted with a diameter of $5 \mu\text{m}$, mimicking the true experimental configurations. As displayed in Fig. 2(c), five critical points represent compression distances from 1 to $5 \mu\text{m}$ (an interval of $1 \mu\text{m}$), respectively. Generally, all models illustrate that the internal stress of the separate springs is uniformly arranged, and there are no severe stress concentrations that may lead to structural collapse, according to color-framed structures shown in Fig. 2(d). With the increase in applied displacements, the top cap keeps flat while the stress at spring-cap connections becomes larger, which can be particularly discovered in the case of $5 \mu\text{m}$. Additional structure enhancements should be paid attention to these areas in order to avoid generations of fatal cracks and flaws.

The spring constant k of rectangle-shaped coils can be theoretically described as follows:²⁸

$$k = \frac{G \cdot t^2 \cdot w^2}{\gamma \cdot n \cdot (2R)^3}, \quad (1)$$

where G is the shear modulus of the material, γ is coefficients (as a function of w/t), and n is the number of coil turns. For univariate analysis, only w is continuously tuned in Figs. 3(a)–3(d) ($t: 4 \mu\text{m}$, $R: 15 \mu\text{m}$), while only R is gradually increased in Figs. 3(e) and 3(f)

($t: 3 \mu\text{m}$, $w: 2 \mu\text{m}$). Note that all the later studies are conducted via identical probe calibrations so as to maintain the consistency of environmental configurations.

At first, we improve w from 4 to $14 \mu\text{m}$ (step size: $2 \mu\text{m}$) to examine their overall mechanical performances. As shown in Fig. 3(a), the force curves (maximum applied force value of $\sim 550 \mu\text{N}$) of six sets of helices exhibit well-separated lineshapes. Their slopes increase with a rise of w , which are both captured over compression and recovery procedures. The further analysis in (b) spotlight one-order sensitivities of k ranging from 9.9 to $108.2 \mu\text{N}/\mu\text{m}$. According to Eq. (1), although k and w^2 do not follow a strictly linear relationship (γ in a range from about 5.2 to 8.0), good agreement (fitting $R^2 \sim 98.38\%$) between measured data and linearly fitted value ($\sim w^2$, see the dashed line) is gained, indicating that the spring equation could be assisted to fast design helical geometries with targeted k .

Next, we focus on a narrow w range [4.0 – $5.0 \mu\text{m}$ with an increment of $0.2 \mu\text{m}$, see the shadowed area in (b)] to explore the structure behavior. The corresponding measurement data are gathered in Figs. 3(c) and 3(d). Here, highly similarities are found, compared to the previous experimentations, where k (as a function of w) upgrades from 9.9 to $17.9 \mu\text{N}/\mu\text{m}$. Despite small offsets, the measurements still follow a data trend akin to Eq. (1), being proportional to w^2 (fitting $R^2 \sim 93.37\%$). More importantly, the diagrams in the orange box indeed demonstrate that k could be accurately controlled to an averaged resolution of $\sim 1.6 \mu\text{N}/\mu\text{m}$ even under a broad range of two orders of magnitude.

Likewise, the variations of coil outer radius R are assumed to alter spring properties as well. The information containing R from 12 to $18 \mu\text{m}$ (a gap of $2 \mu\text{m}$) is set out in Fig. 3(e), together with the detailed investigations of k values summarized in (f). In line with expectations,

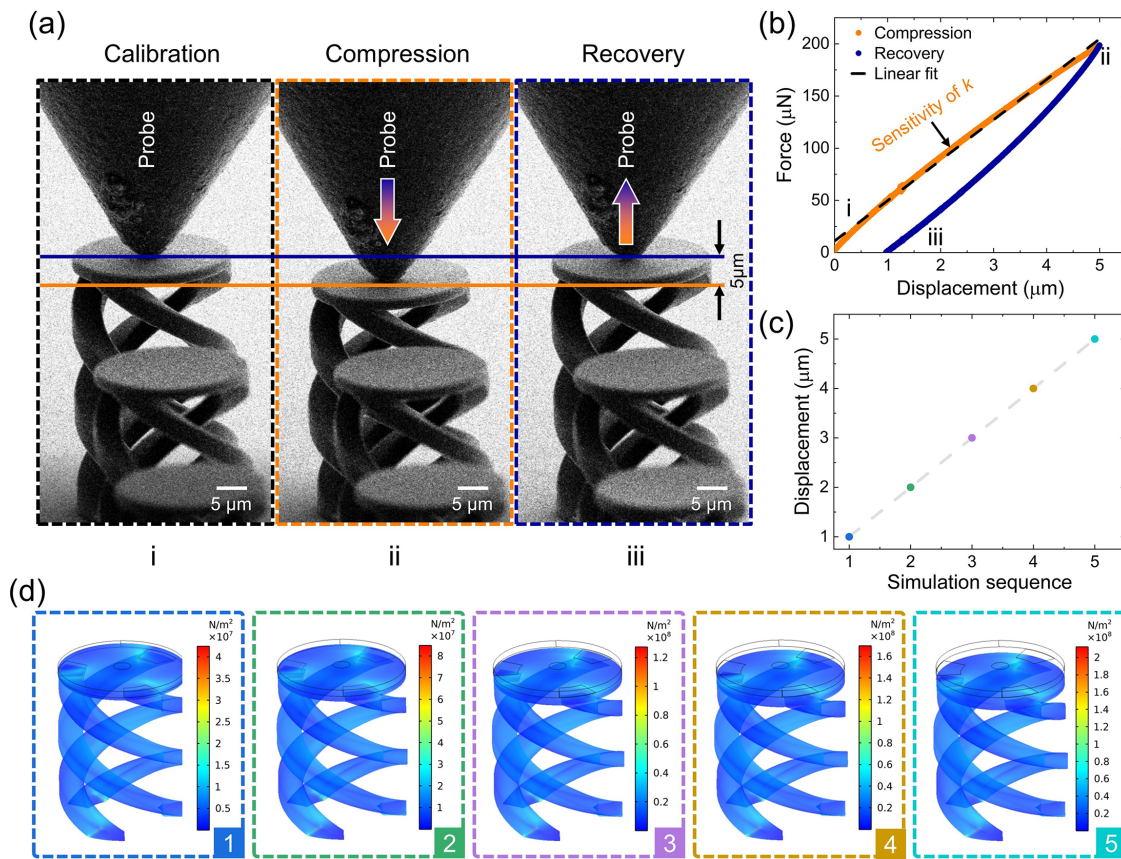


FIG. 2. The *in situ* mechanical characterizations of a spring (geometry parameters of $R = 15 \mu\text{m}$, $w = 7 \mu\text{m}$, and $t = 4 \mu\text{m}$, $H = 60 \mu\text{m}$, $N = 3$ and $n = 1$) accompanied by simulation models. (a) Three consecutive images showing the detailed configurations and general process. A complete experimental cycle includes three phases titled as probe calibration (see the bottom label of “i”), structure compression (“ii”), and recovery (“iii”), respectively. (b) The force-vs-displacement curve obtained from the indenter. Two color-coded lines correspond to measurement procedures [orange: compression procedure (loading), blue: recovery process (unloading)], and the sensitivity of k (unit: $\mu\text{N}/\mu\text{m}$) refers to the linear fit value throughout loading step. (c) Numerical simulation sequences vs. applied displacements. The structural parameters are adopted from (a), and specific five values (indicated by color-coded markers) are selected to match the experimental conditions. (d) Finite-element analysis on stress distributions of micro-springs with compression distances from $1 \mu\text{m}$, $2 \mu\text{m}$, $3 \mu\text{m}$, $4 \mu\text{m}$, to $5 \mu\text{m}$, respectively.

the spring becomes softer and easier to be compressed with the growth of R , and k steadily drops from 4.6 to $1.5 \mu\text{N}/\mu\text{m}$ (averaged resolution down to $1.0 \mu\text{N}/\mu\text{m}$), matching the fitted values ($\sim R^{-3}$) of Eq. (1) (fitting $R^2 \sim 97.57\%$).

Table II presents relevant springs' sensitivities together with commercial AFM tips (Bruker Corp.²⁹) Since varied assessment scenarios may introduce spring sensitivity shifts, we list the relevant characterization methods in the table as well. Although our current TPP-produced spring obtains the second smallest k , further appropriate geometry modifications on both w and R should continue to lower k close to Ref. 21 as well as AFM tips. To lower k down to the next order, probably algorithm-aid structure designs³⁰ will be of great help. In addition, here the k span approaches counterparts of commercially available AFM cantilevers, representing coefficients that may benefit tremendous applications of micro-scale force-sensing. Above all, we do believe that our results represent the widest sensitivities range with accurate coefficient regulation of 3D micro-springs achieved so far.

Finally, the stabilities of the helix spring are probed by consecutive measurements on one micro-spring ($w = 7 \mu\text{m}$, $R = 15 \mu\text{m}$, $t = 4 \mu\text{m}$, $H = 60 \mu\text{m}$, $N = 3$, $n = 1$). The experimental results provided in Fig. 4(a) show that the force curves of five cycles overlap with each other, and k stays at the same value of $\sim 38.63 \pm 0.38 \mu\text{N}/\mu\text{m}$. The tiny fluctuations ($< 1\%$) of sensitivities confirm that our proposed structure exhibits outstanding mechanical stability and strong recovery ability despite various compressions.

In summary, we have designed and implemented helix-based force-sensing micro-springs with fine tuned sensitivities and strong design flexibilities. To improve TPP-empowered fabrications, the post-processing on hollow structures is developed by combining violet light treatment with a special cleaning fluid. Over two orders of magnitude (1.5 to $108.2 \mu\text{N}/\mu\text{m}$) of spring sensitivities k alongside a controlled resolution (down to $1 \mu\text{N}/\mu\text{m}$) are steadily obtained by altering the helix geometries (i.e., R and w), reaching comparable sensitivities of the commercial AFM cantilever tips. In addition, the multiple compression tests together with real-time SEM observations highlight the

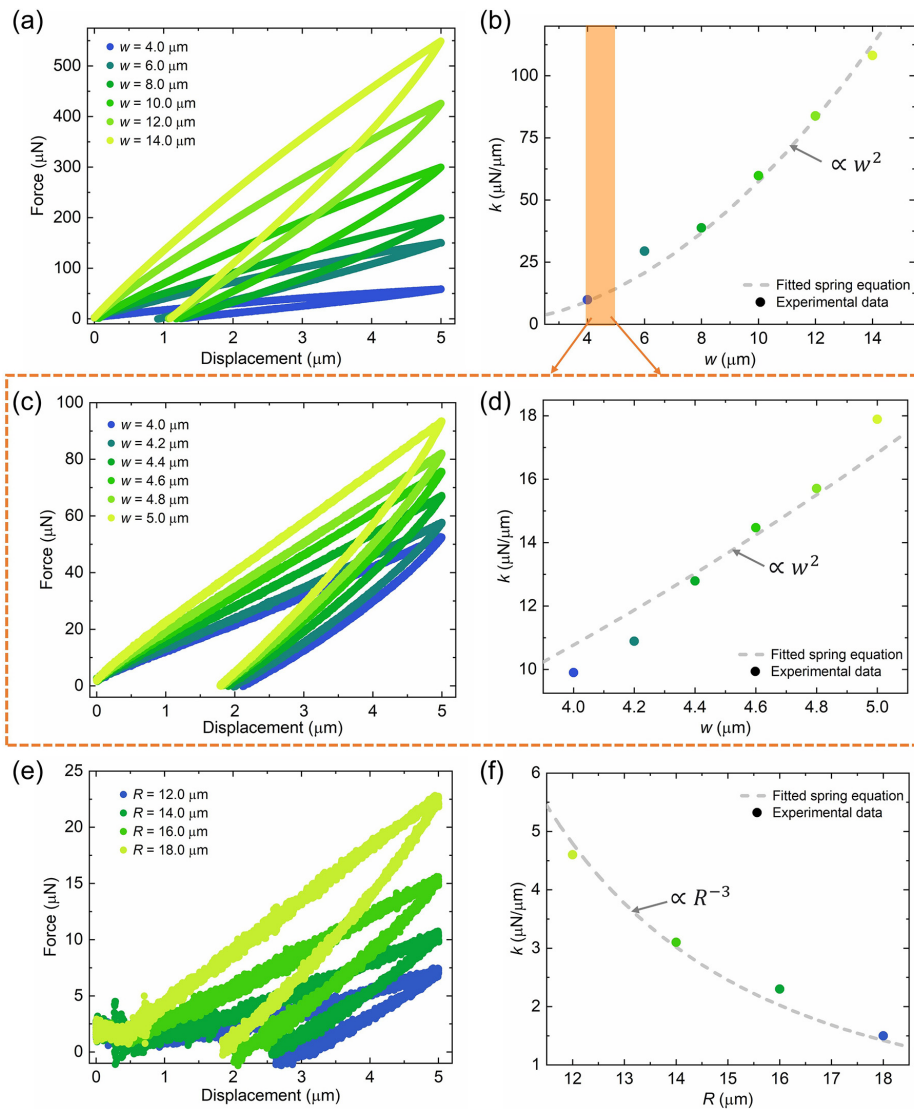


FIG. 3. Benchmark studies on micro-springs (helix number $N=3$, coil turn $n=1$) via univariate geometrical variations in w or R . All the k are designated as linear fit numbers over structure compressions process. (a) and (b) The force–displacement curves (left) of springs alongside their sensitivity analysis (right) under a wide scope of w . The dashed line in (b) is the fitted values (proportional to w^2) using Eq. (1). Spring parameters of t , H and R are set as constants of 4 and $60 \mu\text{m}$, and $15 \mu\text{m}$, respectively. (c) and (d) A closer inspection of sensing performances by altering w within $1 \mu\text{m}$ range. (e) and (f) The helical structure evaluations by solely increasing R . Again, the gray-dashed line ($\sim R^{-3}$) in (f) corresponds to the data fitted by the spring equation. Here t , H , and w are fixed at 3, 40, and $2 \mu\text{m}$, respectively.

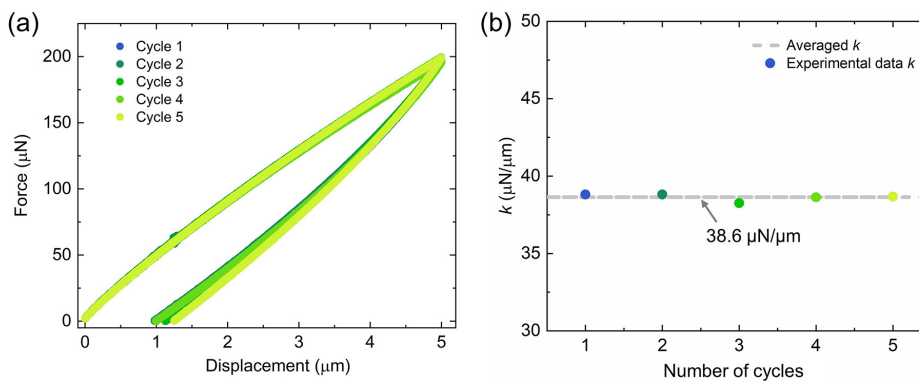


FIG. 4. Repeated compression and recovery examinations on a helical spring ($w: 7 \mu\text{m}$, $R: 15 \mu\text{m}$, $t: 4 \mu\text{m}$, $H: 60 \mu\text{m}$, $N: 3$, $n: 1$). (a) The force–displacement measurements over five complete cycles. (b) The sensitives of k with an averaged value of about $38.6 \mu\text{N}/\mu\text{m}$ (indicated by the dashed line).

TABLE II. Summary of the reported mechanical performances on spring structures.

Reference	Characterization method	Reported minimum k	Characterized range of k
17	Home-made platform and SEM	10 $\mu\text{N}/\mu\text{m}$	10–50 $\mu\text{N}/\mu\text{m}$
19	Home-made platform	~ Several $\mu\text{N}/\mu\text{m}$...
21	AFM	~ 0.1 $\mu\text{N}/\mu\text{m}$...
22	Home-made platform	~ 10.52 $\mu\text{N}/\mu\text{m}$...
Commercial AFM tips ²⁹	...	0.2 $\mu\text{N}/\mu\text{m}$	0.2–40 $\mu\text{N}/\mu\text{m}$
This work	<i>In situ</i> indenter	1.5 $\mu\text{N}/\mu\text{m}$	1.5–108.2 $\mu\text{N}/\mu\text{m}$

strong recovery abilities of triple-helix platforms. All these results summarized here clearly demonstrate the superior fabrication abilities of the improved TPP as well as the excellent mechanical performances of our spring-shaped microstructures.

Particularly, incorporating high-precision TPP printing, we can principally implement any microscale spring-based force sensors with tunable coefficients to cope with broad applications^{31,32} including microelectromechanical systems,^{33–35} bio-material inspections,^{36,37} and force spectrometers.³⁸ For instance, in biological examinations, the detected forces many exist in a vast scope from a few piconewton (pN) (e.g., notch activation at the cell–cell interface requires forces between 4 and 12 pN³⁹) to micronewton (μN) (e.g., the adhesion force of 1.6 μN was measured between HeLa cells and a fibronectin-coated surface.)⁴⁰ In addition, benefiting from the spring-cap arrangement, the proposed micro-structures could be adopted as a platform for application scenarios like miniaturized pressures sensors, where the commercial AFM tips are difficult to be implemented. Due to the excellent compatibility of TPP, the spring-caps can also be transferred on unconventional substrates (e.g., optical fibers³⁷) for highly integrated probes. Therefore, our concept would generate great impact in a variety of frontier research fields such as bio-sensing, where microscale accurate force detections are urgently needed.

See the [supplementary material](#) for more SEM image of a spring array and a video showing the spring characterizations via an *in situ* nano-indenter.

The work was supported by the National Natural Science Foundation of China (Nos. 62005224, 61927820, 51905446, and 51975211), the National Key Research and Development Program of China (No. 2017YFA0205700), and Shanghai Rising-Star Program (No. 20QA1402500). The authors thank Westlake Center for Micro/Nano Fabrication for the facility support and technical assistance. N.W. and X.G.S. thank Mrs. Yingying Huang and Mrs. Pin Wang for communications of experimental characterizations. The authors also appreciate useful discussions with Dr. Xiaorui Zheng and Dr. Yang Gao.

AUTHOR DECLARATIONS

Conflict of Interest

The authors have no conflicts to disclose.

DATA AVAILABILITY

The data that support the findings of this study are available from the corresponding author upon reasonable request.

REFERENCES

- R. Hooke, “De potentia restitutiva, or of spring explaining the power of springing bodies,” in *Sixth Cutler Lecture* (John Martyn, 1678), Vol. 1678, pp. 331–356; available at <https://ota.bodleian.ox.ac.uk/repository/xmlui/handle/20.500.12024/A44322>.
- Y. Chen, “Nanofabrication by electron beam lithography and its applications: A review,” *Microelectron. Eng.* **135**, 57–72 (2015).
- M. L. Tseng, Z.-H. Lin, H. Y. Kuo, T.-T. Huang, Y.-T. Huang, T. L. Chung, C. H. Chu, J.-S. Huang, and D. P. Tsai, “Stress-induced 3D chiral fractal metasurface for enhanced and stabilized broadband near-field optical chirality,” *Adv. Opt. Mater.* **7**, 1900617 (2019).
- D. Zhao, A. Han, and M. Qiu, “Ice lithography for 3D nanofabrication,” *Sci. Bull.* **64**, 865–871 (2019).
- N. Wang, M. Zeisberger, U. Hübner, and M. A. Schmidt, “Nanotrimer enhanced optical fiber tips implemented by electron beam lithography,” *Opt. Mater. Express* **8**, 2246–2255 (2018).
- Y. Hong, D. Zhao, J. Wang, J. Lu, G. Yao, D. Liu, H. Luo, Q. Li, and M. Qiu, “Solvent-free nanofabrication based on ice-assisted electron-beam lithography,” *Nano Lett.* **20**, 8841–8846 (2020).
- J.-F. Xing, M.-L. Zheng, and X.-M. Duan, “Two-photon polymerization micro-fabrication of hydrogels: An advanced 3D printing technology for tissue engineering and drug delivery,” *Chem. Soc. Rev.* **44**, 5031–5039 (2015).
- K.-S. Lee, D.-Y. Yang, S. H. Park, and R. H. Kim, “Recent developments in the use of two-photon polymerization in precise 2D and 3D microfabrications,” *Polym. Adv. Technol.* **17**, 72–82 (2006).
- Q. Geng, D. Wang, P. Chen, and S.-C. Chen, “Ultrafast multi-focus 3D nanofabrication based on two-photon polymerization,” *Nat. Commun.* **10**, 2179 (2019).
- M. Deubel, G. Von Freymann, M. Wegener, S. Pereira, K. Busch, and C. M. Soukoulis, “Direct laser writing of three-dimensional photonic-crystal templates for telecommunications,” *Nat. Mater.* **3**, 444–447 (2004).
- J. K. Gansel, M. Thiel, M. S. Rill, M. Decker, K. Bade, V. Saile, G. von Freymann, S. Linden, and M. Wegener, “Gold helix photonic metamaterial as broadband circular polarizer,” *Science* **325**, 1513–1515 (2009).
- J. K. Hohmann, M. Renner, E. H. Waller, and G. von Freymann, “Three-dimensional μ -printing: An enabling technology,” *Adv. Opt. Mater.* **3**, 1488–1507 (2015).
- K. Sugioka and Y. Cheng, “Femtosecond laser three-dimensional micro- and nanofabrication,” *Appl. Phys. Rev.* **1**, 041303 (2014).
- T. Abele, T. Messer, K. Jahnke, M. Hippler, M. Bastmeyer, M. Wegener, and K. Göpfrich, “Two-photon 3D laser printing inside synthetic cells,” *Adv. Mater.* **34**, 2106709 (2022).
- T. Bückmann, N. Stenger, M. Kadic, J. Kaschke, A. Frölich, T. Kennerknecht, C. Eberl, M. Thiel, and M. Wegener, “Tailored 3d mechanical metamaterials made by dip-in direct-laser-writing optical lithography,” *Adv. Mater.* **24**, 2710–2714 (2012).
- J. Purtov, A. Verch, P. Rogin, and R. Hensel, “Improved development procedure to enhance the stability of microstructures created by two-photon polymerization,” *Microelectron. Eng.* **194**, 45–50 (2018).
- M. Power, A. J. Thompson, S. Anastasova, and G.-Z. Yang, “A monolithic force-sensitive 3D microgripper fabricated on the tip of an optical fiber using 2-photon polymerization,” *Small* **14**, 1703964 (2018).

- ¹⁸A. Nishiguchi, A. Mourran, H. Zhang, and M. Moller, "In-gel direct laser writing for 3D-designed hydrogel composites that undergo complex self-shaping," *Adv. Sci.* **5**, 1700038 (2018).
- ¹⁹A. J. Thompson, M. Power, and G.-Z. Yang, "Micro-scale fiber-optic force sensor fabricated using direct laser writing and calibrated using machine learning," *Opt. Express* **26**, 14186–14200 (2018).
- ²⁰S. Hu, X. Cao, T. Reddyhoff, D. Puhan, S.-C. Vladescu, J. Wang, X. Shi, Z. Peng, A. J. DeMello, and D. Dini, "Liquid repellency enhancement through flexible microstructures," *Sci. Adv.* **6**, eaba9721 (2020).
- ²¹S. Ushiba, K. Masui, N. Taguchi, T. Hamano, S. Kawata, and S. Shoji, "Size dependent nanomechanics of coil spring shaped polymer nanowires," *Sci. Rep.* **5**, 17152 (2015).
- ²²B. Li, B. Gil, M. Power, A. Gao, S. Treratanakulchai, S. Anastasova, and G.-Z. Yang, "Carbon-nanotube-coated 3D microspring force sensor for medical applications," *ACS Appl. Mater. Interfaces* **11**, 35577–35586 (2019).
- ²³E. ToolBox, see https://www.engineeringtoolbox.com/surface-tension-d_962.html for "Liquids Surface Tension—Water, Mercury, Oils and More (2005)" (last accessed November 16, 2021).
- ²⁴D. Zhu and R. Verduzco, "Ultralow surface tension solvents enable facile cof activation with reduced pore collapse," *ACS Appl. Mater. Interfaces* **12**, 33121–33127 (2020).
- ²⁵R. Deshpande, D.-W. Hua, D. M. Smith, and C. J. Brinker, "Pore structure evolution in silica gel during aging/drying. III. Effects of surface tension," *J. Non-Cryst. Solids* **144**, 32–44 (1992).
- ²⁶X. Li, S. Bi, G. Zhao, P. Lu, and Y. Wang, "Experiment on liquid density and surface tension of nonafluorobutylmethylether," *J. Xi'an Jiaotong Univ.* **45**, 70–73 (2011).
- ²⁷M. W. Seto, B. Dick, and M. J. Brett, "Microsprings and microcantilevers: Studies of mechanical response," *J. Micromech. Microeng.* **11**, 582 (2001).
- ²⁸B. Wen, *Machine Design Handbook* (China Machine Press, Beijing, China, 2009).
- ²⁹B. Corp., see <https://www.brukerafmprobes.com/> for "Bruker AFM Probes Scanning Probe and Atomic Force Instrumentation (2021)" (last accessed November 12, 2021).
- ³⁰N. Wang, W. Yan, Y. Qu, S. Ma, S. Z. Li, and M. Qiu, "Intelligent designs in nanophotonics: From optimization towards inverse creation," *PhotonIX* **2**, 1–35 (2021).
- ³¹E. Bo, X. Ge, Y. Luo, X. Wu, S. Chen, H. Liang, S. Chen, X. Yu, P. Shum, J. Mo *et al.*, "Cellular-resolution *in vivo* tomography in turbid tissue through digital aberration correction," *PhotonIX* **1**, 9 (2020).
- ³²R. Fu, Y. Su, R. Wang, X. Lin, X. Jin, H. Yang, W. Du, X. Shan, W. Lv, and G. Huang, "Single cell capture, isolation, and long-term *in situ* imaging using quantitative self-interference spectroscopy," *Cytometry, Part A* **99**, 601–609 (2021).
- ³³W. Niu, L. Fang, L. Xu, X. Li, H. Ruikun, D. Guo, and Z. Qi, "Summary of research status and application of mems accelerometers," *J. Comput. Commun.* **06**, 215 (2018).
- ³⁴H. T. Le, R. I. Haque, Z. Ouyang, S. W. Lee, S. I. Fried, D. Zhao, M. Qiu, and A. Han, "Mems inductor fabrication and emerging applications in power electronics and neurotechnologies," *Microsyst. Nanoeng.* **7**, 59 (2021).
- ³⁵J. U. Surjadi, L. Gao, H. Du, X. Li, X. Xiong, N. X. Fang, and Y. Lu, "Mechanical metamaterials and their engineering applications," *Adv. Eng. Mater.* **21**, 1800864 (2019).
- ³⁶M. R. Nejadnik, H. C. van der Mei, W. Norde, and H. J. Busscher, "Bacterial adhesion and growth on a polymer brush-coating," *Biomaterials* **29**, 4117–4121 (2008).
- ³⁷M. Zou, C. Liao, S. Liu, C. Xiong, C. Zhao, J. Zhao, Z. Gan, Y. Chen, K. Yang, D. Liu *et al.*, "Fiber-tip polymer clamped-beam probe for high-sensitivity nano-force measurements," *Light: Sci. Appl.* **10**, 171 (2021).
- ³⁸K. C. Neuman and A. Nagy, "Single-molecule force spectroscopy: Optical tweezers, magnetic tweezers and atomic force microscopy," *Nat. Methods* **5**, 491–505 (2008).
- ³⁹F. Chowdhury, I. T. Li, T. T. Ngo, B. J. Leslie, B. C. Kim, J. E. Sokoloski, E. Weiland, X. Wang, Y. R. Chemla, T. M. Lohman *et al.*, "Defining single molecular forces required for notch activation using nano yoyo," *Nano Lett.* **16**, 3892–3897 (2016).
- ⁴⁰P. Saha, T. Duanis-Assaf, and M. Reches, "Fundamentals and applications of fluidfm technology in single-cell studies," *Adv. Mater. Interfaces* **7**, 2001115 (2020).